CrossMark

Impulse response analysis of carrier-modulated multiband RF-interconnect (MRFI)

Yanghyo Kim[1,2] · Wei-Han Cho[1] · Yuan Du[1] · Jason Cong[1] · Tatsuo Itoh[1] ·
Mau-Chung Frank Chang[1,3]

Abstract Impulse response of energy-efficient multiband RF-interconnect (MRFI) is analyzed to quantify its information capacity for transmitting digital data via various types of physical wires. Our analyses in frequency domain (also transferrable to time domain if needed) indicate that a baseband-equivalent impulse response can be established for MRFI under coherently communicated systems. We can further express such response in an explicit form for MRFI with low-pass transmission nature. It also reveals its distinct capability in signal equalization as a result of its RF-carrier down-conversion process. Furthermore, the analysis offers a guidance of how to construct baseband-equivalent impulse response when transmission lines contain non-ideal effects such as frequency notches and in-band ripples.

✉ Yanghyo Kim
   rod.kim@jpl.nasa.gov

   Wei-Han Cho
   hihiwill@gmail.com

   Yuan Du
   yuandu@ucla.edu

   Jason Cong
   cong@cs.ucla.edu

   Tatsuo Itoh
   itoh@seas.ucla.edu

   Mau-Chung Frank Chang
   mfchang@ee.ucla.edu

[1] University of California, Los Angeles, CA, USA

[2] Jet Propulsion Laboratory, Pasadena, CA, USA

[3] National Chiao Tung University, Hsinchu City, Taiwan

1 Introduction

Over the years, systems such as asymmetric digital subscriber lines (ADSL) and very high-speed digital subscriber lines (VHDSL) have proven the vital role of passband signaling in wireline data communication area. Accordingly, academia/industry has conducted numerous research to study the performance of information carrying passband signals through wires/cables [1–8]. As part of the continuing evolution aimed at multi-gigabit per second (Gb/s) wireline communication, a similar passband signaling, also known as multiband RF-interconnect (MRFI), has been proposed to transfer multiple baseband data simultaneously by way of carrier-modulated RF channels [9–15]. As a common approach, previous works have adopted an on–off keying (OOK) modulation with self-mixing down-conversion architecture for RF channels and demonstrated data rate of multi-Gb/s through shared on-chip or off-chip transmission lines. An OOK with self-mixing non-coherent architecture benefits energy efficiency because a receiver does not require additional synthesizer or carrier synchronization [16, 17]. Unfortunately, the non-coherent system lacks the ability to split signal space into in-phase (I) and quadrature-phase (Q) domains for RF channels. In order to maximize spectral efficiency, recent research has developed multi-level, multi-band, and IQ processing coherent transceiver architecture, which is the main interest of this paper [18–23].

⊈ Springer

A generalized block diagram of coherent RFI system is illustrated in Fig. 1. Note that the number of RF channels and selection of carrier frequency are flexible, and multi-level signaling can be applied to each data path by adding digital-to-analog converter (DAC) in transmitter (TX) and analog-to-digital converter (ADC) in receiver (RX).

Although previous research has suggested the potential of deploying MRFI system in wireline data communication platform, no theoretical background has been provided to evaluate the information capacity of given transmission line. Transmission lines are known to be dispersive or band-limited mainly because conductive loss and dielectric loss increase as frequency of operation increases. Typically, the frequency where loss is 3–6 dB offers a rough estimate of how much data transmission line can convey. This 3–6 dB estimation can change depending on system requirements, but this paper assumes -3 dB frequency as the bandwidth of transmission line. More advanced methods include sending a short pulse and measuring pre/post cursor, or one step further, evaluating an eye-diagram by transmitting random bit sequences. The underlying assumption to the methods above is that either a scattering parameter or linear time-invariant (LTI) impulse response of transmission line is readily available.

One of the major goals of this paper is to come up with an exact expression of baseband-equivalent impulse response in frequency domain when coherent MRFI transceivers communicate through transmission lines that support transverse electromagnetic (TEM) mode of propagation. A baseband-equivalent impulse response fully captures the physical characteristics of carrier frequency dependent passband signals through physical channels and translates as if the system functions in baseband domain. Because of its baseband equivalency, direct frequency response comparison between various carrier frequencies, or comparison between baseband-only signaling versus MRFI signaling, is possible for a given transmission line. The proposed impulse response analysis will not consider performance of electronics but focus only on physical properties of transmission lines including loss, non-idealities, signal-to-noise (SNR) trade-off, and eye-diagram characteristics.

2 Baseband-equivalent impulse response

One of the RF channels from Fig. 1 is emphasized with annotations in Fig. 2(a). The system diagram in Fig. 2(a) contains only an in-phase path, but a quadrature path could always be added for the same analysis. Also, time domain and frequency domain symbols are written with lower case and upper case letters, respectively. An input data $x(t)$ modulates carrier (ω_0) via up-converter and travels through a transmission line $h(t)$. A down-converter then de-modulates an incoming signal with receiver side local oscillator (LO). A fixed amount of extra LO phase, which is directly calculated from transmission line delay at the carrier frequency, is added to receiver LO to synchronize phase
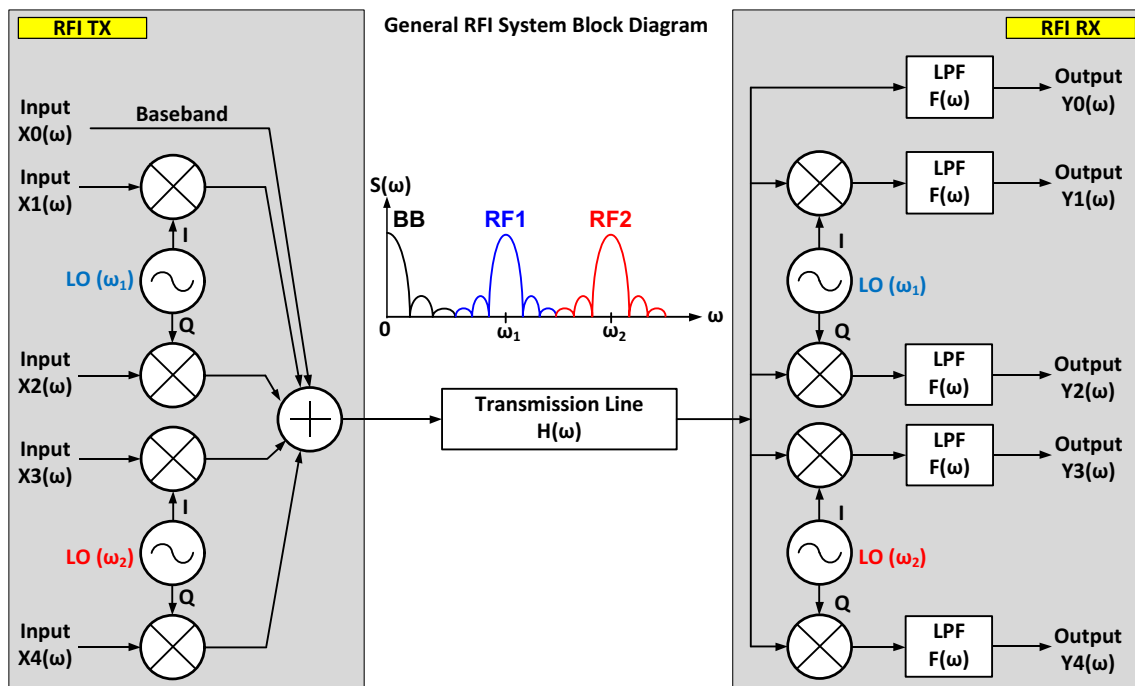

Fig. 1 Generalized block diagram of coherent RFI system

Fig. 2 a Coherent based full transmitter and receiver system includes up-converter, down-converter, local oscillators, and low-pass filter. Two local oscillators are assumed to be phase and frequency synchronized in the transmitter and receiver side. **b** The full system is replaced by a baseband-equivalent transmission line channel as an impulse response. **c** The process of frequency domain calculation is shown in alphabetical order that was listed in (**a**). Note from the property of LTI system that time domain multiplication becomes frequency domain convolution, and time domain convolution becomes frequency domain multiplication
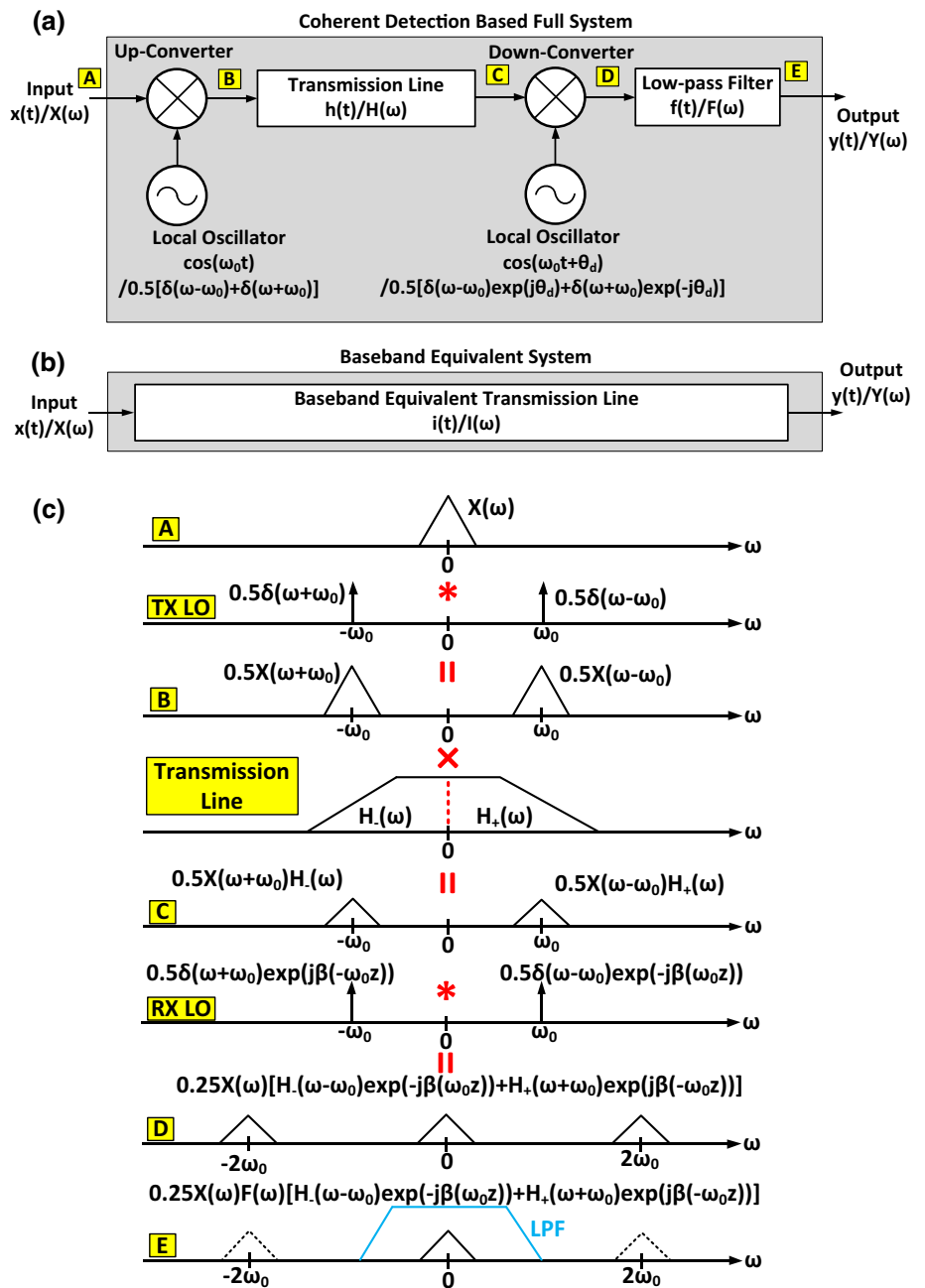
between transmitter and receiver. A method of synchronization is beyond the discussion of this paper, and the phase and frequency between transmitter and receiver are assumed to be synchronized. In the last stage, a low-pass filter (LPF) filters out the residue of $2\omega_0$ component generated from the down-conversion process. An ultimate objective is to capture the non-linear property of transmission line frequency response and translate to baseband-equivalent impulse response $i(t)$ or $I(\omega)$ model in Fig. 2(b). With an impulse response defined, an output becomes,

$$Y(\omega) = X(\omega)I(\omega) \tag{1}$$

$$y(t) = x(t) * i(t) \tag{2}$$

where $*$ operator indicates a convolution.

Based on the system block diagram, the process of frequency domain computation is built in Fig. 2(c). After solving boundary conditions of a given transmission line, a governing frequency response of electromagnetic field propagating in z-direction can be readily evaluated as,

$$H_+(\omega) = \begin{cases} e^{-\alpha(\omega)z}e^{-j\beta(\omega)z} & (\omega > 0) \\ 0 & (\omega < 0) \end{cases}$$

$$H_-(\omega) = \begin{cases} 0 & (\omega > 0) \\ e^{-\alpha(\omega)z}e^{+j\beta(\omega)z} & (\omega < 0) \end{cases}$$

$$H(\omega) = H_+(\omega) + H_-(\omega) \tag{3}$$

where α is an attenuation constant, β is a propagation constant, and z is length of transmission line [24]. $H(\omega)$ divides into $(+)$ and $(-)$ components to process a conjugate symmetric property of frequency response. Attenuation constant α and propagation constant β are frequency-dependent, geometry-dependent, and transmission-line-type-dependent. To demonstrate the idea, an input spectrum $X(\omega)$ and transmission line frequency response $H(\omega)$ are configured arbitrarily in Fig. 2(c). A key message in this figure is to include and calculate the negative frequency spectral portion throughout the procedure. To summarize the process at each node,

A: $X(\omega)$ (4)

TX LO: $\dfrac{1}{2}[\delta(\omega + \omega_0) + \delta(\omega - \omega_0)]$ (5)

B: $\dfrac{1}{2}[X(\omega + \omega_0) + X(\omega - \omega_0)]$ (6)

C: $\dfrac{1}{2}[X(\omega + \omega_0)H_-(\omega) + X(\omega - \omega_0)H_+(\omega)]$ (7)

RX LO: $\dfrac{1}{2}\left[\delta(\omega + \omega_0)e^{+j\beta(\omega)z} + \delta(\omega - \omega_0)e^{-j\beta(\omega)z}\right]$
$= \dfrac{1}{2}\left[\delta(\omega + \omega_0)e^{+j\beta(-\omega_0)z} + \delta(\omega - \omega_0)e^{-j\beta(\omega_0)z}\right]$ (8)

D: $\left\{\dfrac{1}{2}[X(\omega + \omega_0)H_-(\omega) + X(\omega - \omega_0)H_+(\omega)]\right\}$
$* \left\{\dfrac{1}{2}\left[\delta(\omega + \omega_0)e^{+j\beta(-\omega_0)z} + \delta(\omega - \omega_0)e^{-j\beta(\omega_0)z}\right]\right\}$ (9)

In (8), only a fixed phase portion is extracted from $H(\omega)$ without the amplitude contribution and accumulated to a receiver LO for phase synchronization. Next, (9) can be further expanded to,

$$\frac{1}{4}X(\omega)\left[H_-(\omega - \omega_0)e^{-j\beta(\omega_0)z} + H_+(\omega + \omega_0)e^{+j\beta(-\omega_0)z}\right]$$
$$+ \frac{1}{4}X(\omega + 2\omega_0)H_-(\omega + \omega_0)e^{+j\beta(-\omega_0)z}$$
$$+ \frac{1}{4}X(\omega - 2\omega_0)H_+(\omega - \omega_0)e^{-j\beta(\omega_0)z} \tag{10}$$

The first term in (10) reveals that a baseband spectrum is multiplied by the sum of two frequency shifted transmission line frequency responses. For the latter two terms, it is clear that they are $2\omega_0$ components, and they make the

system in (10) linear time-variant (LTV). Thus, from a mathematical standpoint, an LPF must fully reject the $2\omega_0$ residue in order for a baseband-equivalent frequency response to remain as an LTI system. Practically speaking, the above statement is a reasonable assumption (a consequence of ignoring residue will be explained in the following section), because an LPF needs to be sharp enough to reject inter-channel interference (ICI) between multiple RF channels. Therefore, an output spectrum can be written as,

$$E: Y(\omega) = \frac{1}{4}X(\omega)F(\omega)$$
$$\times \left[H_-(\omega - \omega_0)e^{-j\beta(\omega_0)z} + H_+(\omega + \omega_0)e^{+j\beta(-\omega_0)z}\right] \tag{11}$$

As indicated above, a choice of LPF could greatly affect a baseband-equivalent impulse response. Since the expression of output spectrum is ready, following the definition of impulse response, $x(t) = \delta(t)$, which is $X(\omega) = 1$, can be inserted into (11), and finally a baseband-equivalent impulse response in frequency domain is derived as,

$$I(\omega) = Y(\omega)|_{X(\omega)=1}$$
$$= \frac{1}{4}F(\omega)\left[H_-(\omega - \omega_0)e^{-j\beta(\omega_0)z} + H_+(\omega + \omega_0)e^{+j\beta(-\omega_0)z}\right] \tag{12}$$

There are two important things to highlight. First, a baseband-equivalent impulse response in frequency domain consists of positively shifted and negatively shifted $H(\omega)$ around a carrier frequency. Second, a baseband-equivalent impulse response depends heavily on a carrier frequency. So far, a mathematical framework has been developed. In-depth analysis with examples will deliver intuition in the following sections.

3 Microstrip line

Microstrip lines are an essential part of a high-speed data communication system because of its capability of easy fabrication and integration with other components. Throughout the study, specific dimension, transmission line length, and frequency range will be used because of relation to pulse behavior in time domain. Detailed parameters and geometry of microstrip line are summarized in Fig. 3(a). A common FR4 will be used as substrate material. Note that the same analysis can be applied to any other types of transmission lines such as stripline, co-planar waveguide, twisted pairs, and coax cables, as long as α and β can be provided by analytical calculation, software-aided simulation, or measurement.

(a)

Microstrip Line Parameters	
Trace Width W (µm)	296.9
Dielectric Depth D (µm)	200
Trace Material	Copper
Dielectric Material	FR4
Dielectric Loss Tangent	0.02
Dielectric Constant	4.2

Fig. 3 **a** Cross-section of microstrip line is shown with its parameters. Wave propagates along z-direction. **b** Magnitude response of 10-in microstrip line in linear scale. **c** Phase response of microstrip line
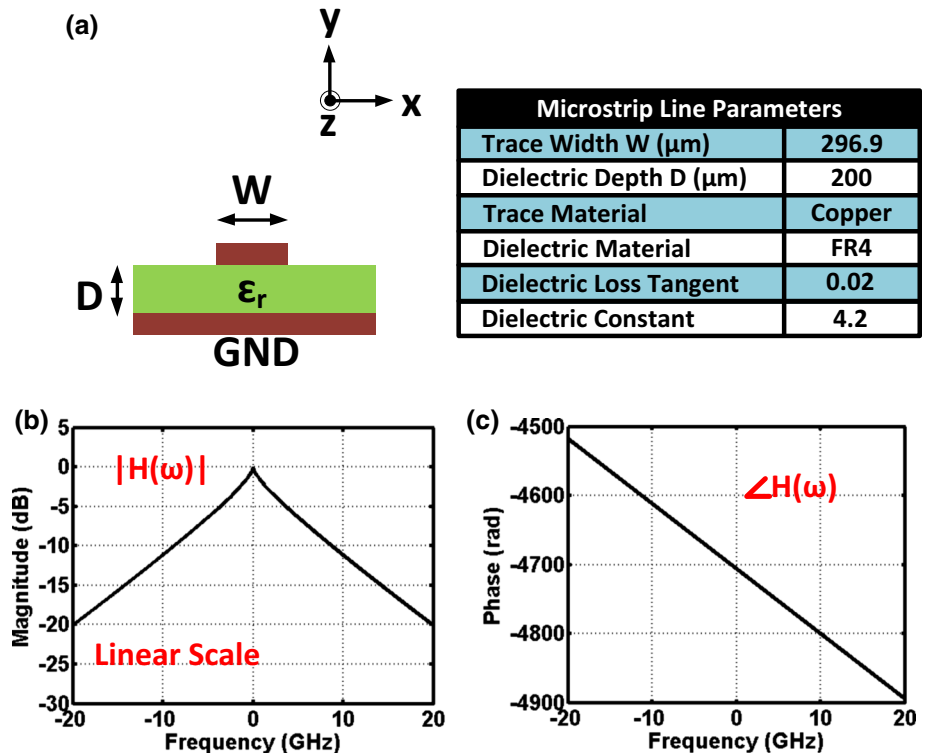
3.1 Attenuation and propagation constant

Instead of repeating the procedure of solving boundary conditions for Maxwell's equations, readily available attenuation and propagation constants of microstrip line are brought from [24],

Free Space Wavenumber: $k_0 = \omega\sqrt{\mu_0\epsilon_0}$ (13)

Propagation Constant: $\beta = \omega\sqrt{\mu_0\epsilon_0\epsilon_r}$ (14)

Surface Resistivity: $R_S = \sqrt{\dfrac{\omega\mu_0}{2\sigma}}$ (15)

Effective Dielectric Constant:

$$\varepsilon_e = \frac{\epsilon_r + 1}{2} + \frac{\epsilon_r - 1}{2}\sqrt{\frac{1}{1 + \frac{12D}{W}}} \qquad (16)$$

Conductive Atten. Constant: $\sigma_c = \dfrac{R_S}{Z_0 W}$ (17)

Dielectric Atten. Constant: $\sigma_d = \dfrac{k_0\epsilon_r(\epsilon_e - 1)tan\delta}{2\sqrt{\epsilon_e}(\epsilon_r - 1)}$ (18)

where μ_0 is permeability in air, μ_r is permeability in medium, ϵ_0 is permittivity in air, ϵ_r is permittivity in medium, σ is conductivity of trace material, D is depth of microstrip line, W is width of microstrip line, and $tan\delta$ is loss tangent of medium. An attenuation constant is the sum of conductive and dielectric attenuation constant. Using the parameters in Fig. 3(a) and transmission line frequency

response in (3), phase and magnitude responses of a 10-in microstrip line are plotted in Fig. 3(b, c). Notice how the phase is asymmetric and magnitude is symmetric around DC. In a general complex number domain, when a system or signal is a real number, the Fourier transform of it becomes conjugate symmetric. A transmission line in time domain is also a real number system, which is why the frequency domain phase and magnitude response appears as conjugate symmetric.

3.2 Baseband-equivalent impulse response in frequency domain

As a reminder from (12), an impulse response in frequency domain is a combination of two frequency responses of microstrip line: one positively shifted, and the other negatively shifted, around a carrier frequency. After applying the frequency response in (3) to (12), each of shifted frequency response over 10-in length (z_1) and resulting baseband-equivalent impulse response are derived as,

$$\frac{1}{4}H_-(\omega - \omega_0)e^{-j\beta(\omega_0)} = \frac{1}{4}e^{-\alpha(\omega-\omega_0)z_1}e^{+j\beta(\omega-\omega_0)z_1}e^{-j\beta(\omega_0)z_1}$$
(19)

$$\frac{1}{4}H_+(\omega + \omega_0)e^{+j\beta(-\omega_0)} = \frac{1}{4}e^{-\alpha(\omega+\omega_0)z_1}e^{-j\beta(\omega+\omega_0)z_1}e^{+j\beta(-\omega_0)z_1}$$
(20)

$$I(\omega) = \frac{1}{4}F(\omega)\left[e^{-\alpha(\omega+\omega_0)z_1}e^{-j\beta(\omega+\omega_0)z_1}e^{+j\beta(-\omega_0)z_1}\right.$$
$$\left. + e^{-\alpha(\omega-\omega_0)z_1}e^{+j\beta(\omega-\omega_0)z_1}e^{-j\beta(\omega_0)z_1}\right] \quad (21)$$

In order to de-embed the effect of LPF, another impulse response expression $B(\omega)$ without LPF is also written as,

$$B(\omega) = \frac{1}{4}\left[e^{-\alpha(\omega+\omega_0)z_1}e^{-j\beta(\omega+\omega_0)z_1}e^{+j\beta(-\omega_0)z_1}\right.$$
$$\left. + e^{-\alpha(\omega-\omega_0)z_1}e^{+j\beta(\omega-\omega_0)z_1}e^{-j\beta(\omega_0)z_1}\right] \quad (22)$$

In the following section, the impact of carrier frequency will be studied in conjunction with the length of transmission line, but for a concept demonstration at the moment, the carrier frequency is deployed at 6 GHz. As shown in Fig. 4(a), a down-conversion by a carrier frequency shifts the frequency response of transmission line around (+) and (−) 6 GHz while preserving its original response. Then, from (22), the magnitude response of $B(\omega)$ is constructed in Fig. 4(b). Interestingly, a frequency peaking at 6 GHz is observable as if the impulse response works as a linear equalizer. Indeed without even solving (22), the peaking behavior can be deduced from Fig. 4(a). Again, a baseband-equivalent impulse response is the sum of two frequency responses (not multiplication), which means the positively shifted frequency response dominantly rises after DC. In Fig. 4(c), frequency response of 3rd order Bessel filter is plotted to implement a linear in-band group delay LPF [19]. The cutoff frequency of LPF in this figure is 8 GHz, but it needs to be adjusted depending on bandwidth of RF channel and ICI.

Using (21), the final magnitude of impulse response $I(\omega)$ is plotted in Fig. 4(d). First of all, the − 3 dB bandwidth of $I(\omega)$ is increased to 6.5 GHz from the original channel bandwidth of 1.8 GHz. Second, DC gain is reduced to − 7.4 dB in exchange of bandwidth, which is

Fig. 4 a Positively and negatively shifted magnitude response. b Frequency response $H(\omega)$ of 10-in microstrip line and its baseband-equivalent impulse response $B(\omega)$, one without LPF, in log scale when carrier frequency is 6 GHz. c Bessel 3rd order LPF frequency response and magnitude response of $B(\omega)$. d Final magnitude response of $I(\omega)$ is plotted with LPF bandwidth of 8 GHz and compared to magnitude response of $H(\omega)$. e Impulse response when LPF bandwidth is 4 GHz. f Impulse response when LPF bandwidth is 12 GHz
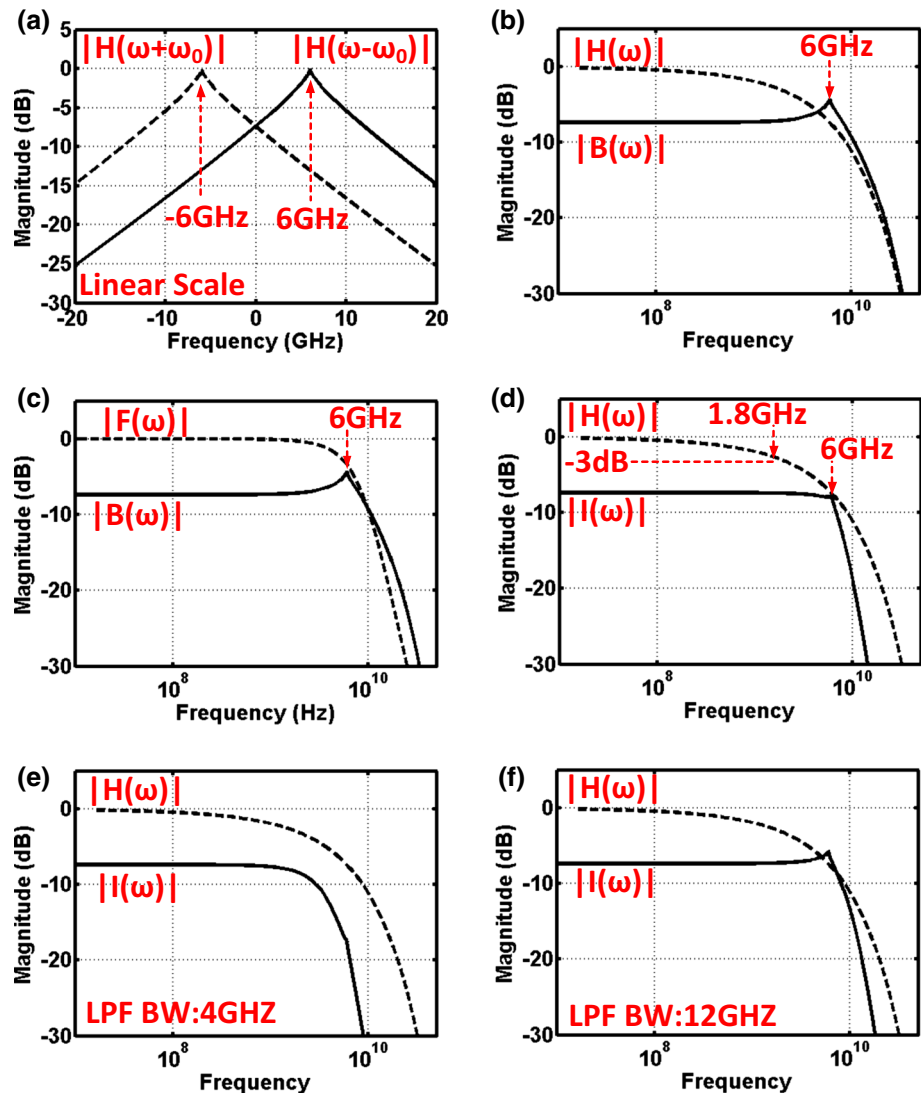
exactly how pre-emphasis is performed. Third, one can also expect that an LPF would eventually determine the bandwidth of impulse response $I(\omega)$ as cutoff frequency of $F(\omega)$ goes below the carrier frequency as shown in Fig. 4(e, f). Lastly, one should keep in mind that a baseband data bandwidth of RF channel cannot be larger than carrier frequency. For instance in Fig. 4(d), the -3 dB bandwidth is higher than 6 GHz, which is the carrier frequency, but it does not mean that an input data rate can be as high as 6 Gb/s bandwidth. Based on the arguments above, higher carrier frequency can achieve higher bandwidth, but at the same time, it loses signal-to-noise ratio (SNR) depending on the length of microstrip line.

As stated in (1), after having established the impulse response of transmission line, an output spectrum can be calculated instantly by multiplying input spectrum and impulse response in frequency domain, as shown in Fig. 5. For instance, imagine 250 ps of single pulse, which is up-converted by carrier frequency of 6 GHz, travels down to a 10-in microstrip line, and gets down-converted by receiver LO of 6 GHz. In frequency domain, it means a sync function is multiplied by the impulse response calculated in Fig. 4(d). Notice the output spectrum rolls off quickly after 6 GHz influenced by the impulse response bandwidth of 6 GHz. Based on the development in (21), this efficient multiplication process in frequency domain can be applied to any carrier frequency or length of microstrip line.

3.3 Time domain impulse response and simulation

In Fig. 6(a), the impulse response of microstrip line in time domain is first calculated by taking an inverse Fourier transform of (21) in MATLAB software. Interestingly, a finite delay of modulated wave through a microstrip line is also reflected in the baseband-equivalent impulse response while the causality condition is kept for the impulse response operable. As suggested in (2), impulse response in time domain is now convoluted with an input pulse to generate an output pulse shown in Fig. 6(c).

In order to prove the validity of frequency domain impulse response expression in (21), a time domain simulation is conducted by stepping through each stage in Fig. 7(a). An up-converter multiplies 250 ps input pulse and 6 GHz carrier signal at node B, and the modulated signal undergoes microstrip line at node C. A down-converter translates to a baseband with $2\omega_0$ residue remained at node D, and a 3rd Bessel filter with 8 GHz cutoff frequency filters out the $2\omega_0$ component at node E. Comparing the output pulse in Fig. 6(c) and the output pulse from time domain simulation in Fig. 7(e), two baseband output signals are almost identical except the fact that there is a slight residue of $2\omega_0$ component left. Therefore, one can expect that the discrepancy would decrease as the cutoff frequency of LPF decreases.

Another crucial advantage of the baseband-equivalent impulse response in time domain is a capability to simulate random bit sequences as input and generate an eye-diagram. A single pulse informs on a degree of dispersion or distortion, but the measure of inter-symbol interference (ISI) requires a random bit pattern. Once impulse response is created, a sequence of randomly combined ones and zeros convolve with the impulse response and produce an eye-diagram by overlapping the output data pattern every bit period. For the given microstrip line in Fig. 3(a) and carrier frequency of 6 GHz, it is clear that 5 Gb/s of data stream is feasible without any equalization, as shown in Fig. 8(b). Provided SNR is high enough, 4 pulse amplitude modulation (4PAM) can double the bandwidth as shown in
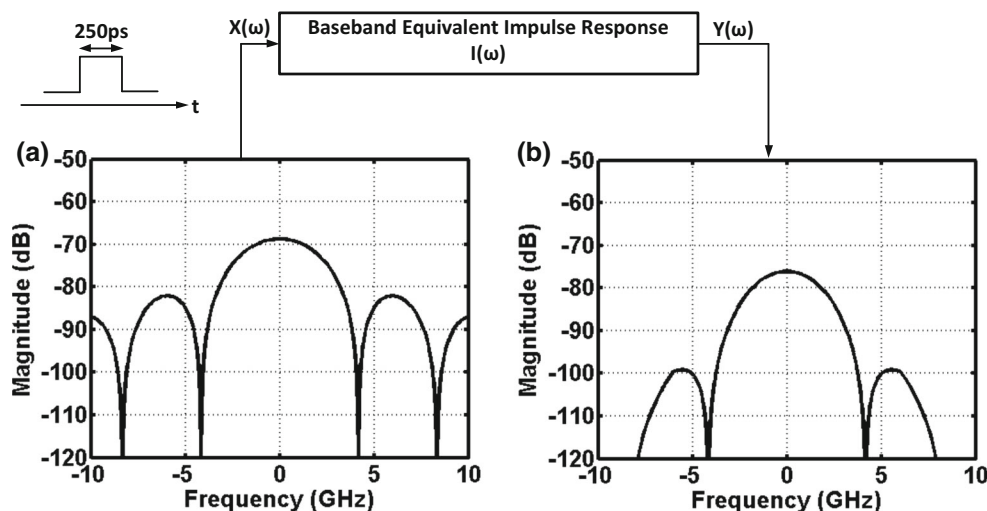

Fig. 5 **a** A 250(ps) baseband pulse is generated at the input of microstrip line. **b** After taking Fourier transform, input spectrum is fed into the baseband-equivalent impulse response of microstrip line, and the output spectrum of pulse is generated instantly by multiplying two spectrums

Fig. 6 **a** Time domain impulse response is calculated on MATLAB from (23). **b** A 250(ps) baseband pulse is generated. **c** Two are convoluted in time domain. A resulting output pulse generated
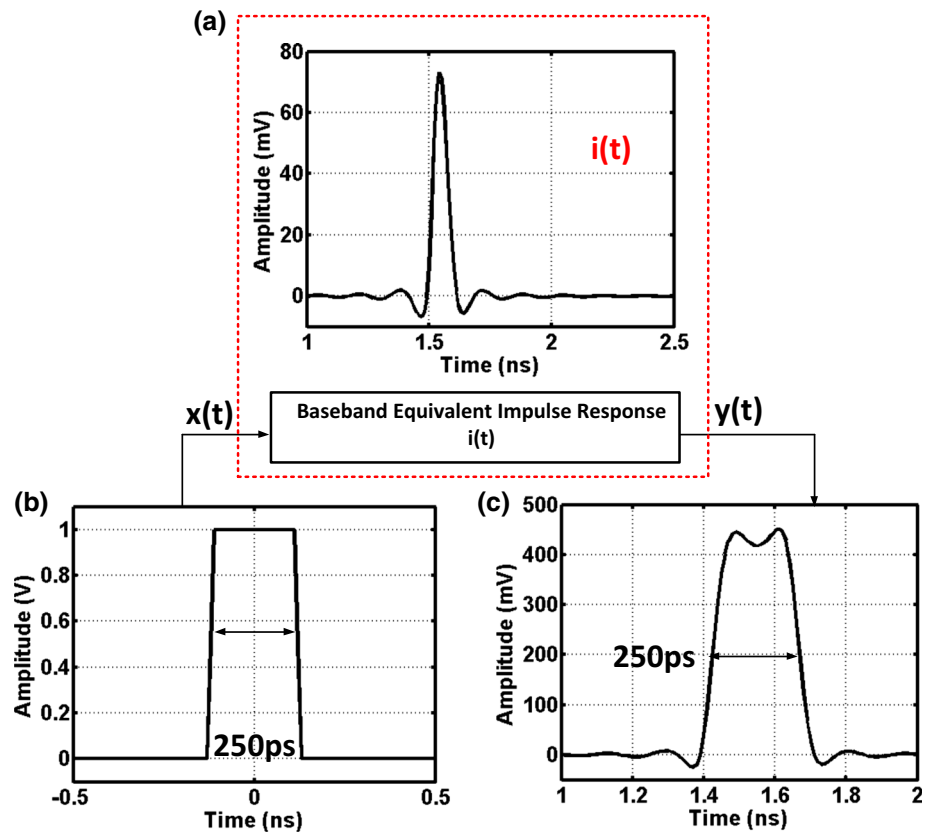

Fig. 8(c, d). Additionally, considering I and Q complex signaling at 6 GHz carrier frequency, which is equivalent to 16 quadrature amplitude modulation (QAM), an aggregate data rate can reach up to 20 Gb/s.

3.4 Effect of carrier frequency

When microstrip line parameters are fixed, conductive and dielectric loss increase as carrier frequency increases. As indicated in the frequency domain study, there is a direct trade-off between achievable bandwidth and system SNR. In Fig. 9(a), an effective baseband bandwidth is increased to 10 GHz with 10 GHz of carrier frequency, but the loss magnitude is also increased to 11.2 dB. In time domain, eye-diagrams of 9 Gb/s random sequence in Fig. 9(b) and 18 Gb/s of 4PAM random sequence in Fig. 9(d) prove the available bandwidth when the carrier frequency is 10 GHz.

According to this simulation, a system power budget has to be considered when choosing carrier frequency, as illustrated in Fig. 10. In the diagram, a receiver sensitivity RX_S is calculated as

$$RX_S(\text{dBm}) = -174 + 10\log(BW) + NF + SNR_{MIN}$$
(23)

where BW is a target data bandwidth, NF is a receiver noise figure, and SNR_{MIN} is the minimum SNR required to achieve bit error rate of less than 10^{-12} for different types

of modulation scheme [25]. In order for a system to be functional under target BER, the power level after loss factor (L_{ω_0}) at particular carrier frequency has to be always larger than RX_S with enough SNR margin.

Up till now, it is assumed that the frequency response of microstrip line has no discontinuity. The above study suggests the following. First, it makes no sense to increase carrier frequency indefinitely; it is preferable to increase within the system power budget to maximize available baseband-equivalent bandwidth. Second, for a system architecture perspective under this transmission line condition, as long as SNR is allowed at the highest possible carrier frequency, it is more *spectrally* efficient to utilize only one carrier frequency instead of multiple RF carriers. This concept is depicted in Fig. 11. For instance, one could decide to generate 5 GHz (ω_1) and 10 GHz (ω_2) carrier frequency. However, because of ICI, each carrier may only carry a maximum bandwidth of 2.5 Gb/s data, total of 5 Gb/s, which is already 4 Gb/s short of what single 10 GHz carrier can offer. Therefore, it is more spectrally efficient to serialize data in baseband domain instead of frequency domain when a frequency response of microstrip line has no non-ideal factors such as frequency notches or ripples.

Fig. 7 **a** Block diagram. **b** Modulated pulse with 6 GHz carrier frequency. **c** Carrier modulated signal after transmission line. **d** Down-converted baseband pulse with $2\omega_0$ residue. **e** Baseband pulse after LPF and comparison to pulse output calculated by impulse response
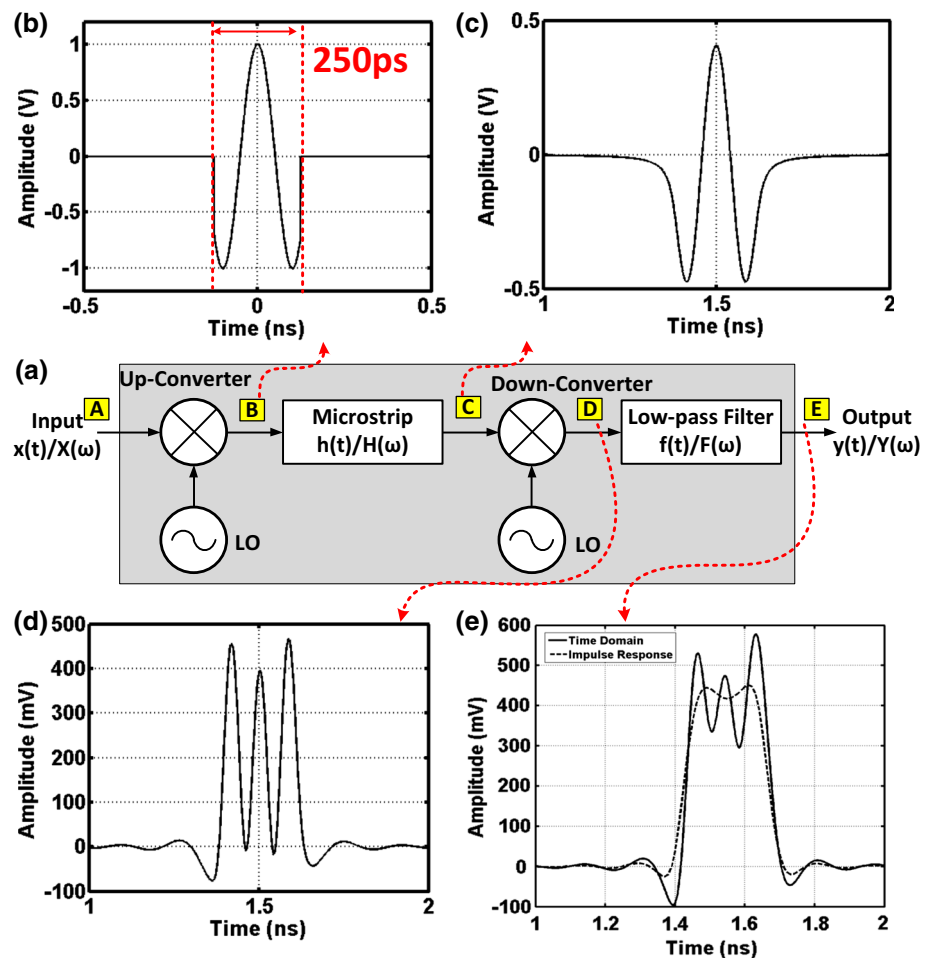
3.5 Microstrip line length and baseband-only signaling bandwidth consideration

Increasing communication distance will limit the bandwidth of microstrip line. The longer the channel, the smaller the bandwidth. As shown in Fig. 12(a), the loss increases as distance increases and the rate of increment in loss also increases as frequency increases because of exponential dependency in frequency response.

Using (3) and expressions from (13) to (18), frequency responses of 2, 6, 10-in microstrip line are plotted in Fig. 12(b), and the bandwidth of each length is estimated at -3 dB loss frequency. From the baseband-only signaling point of view, the frequency response in (3) is already impulse response in frequency domain. Thus, just as in Figs. 6(a) and 8, an inverse Fourier transform is taken from (3) first, and then random sequences are convolved with the generated impulse response in time domain to create eye-diagrams. For the case of a 2-in microstrip line, the 3 dB bandwidth reaches 14 GHz, and the channel is capable of sending 14 Gb/s of random sequence without any help of equalization. Therefore, in

this case, there is no reason to produce a carrier frequency below 14 GHz. The same principle applies to longer channels. For 6- and 10-in case, baseband-only signaling is able to transfer 3.7 and 1.8 Gb/s, respectively. In Fig. 12(f), the eye-diagram is almost closed when 18 Gb/s of baseband-only signaling is passed through a 10-in microstrip line, while the IQ based RFI system with carrier frequency at 10 GHz can successfully transfer 18 Gb/s of data as studied in Fig. 9(b).

In order to achieve wide-open eye-diagrams, one can choose either equalization scheme based on baseband-only signaling or RFI scheme. Many equalization schemes have been proposed and are being widely exploited in industry and academia for high-speed data communication applications [26–29]. It is not the interest of this paper to compare the two system architectures nor determine at what point equalization is required, because the figure of merit, which is energy spent per achieved data bandwidth, heavily depends on device technology scaling, type of equalization, length of transmission line (loss at target bandwidth), SNR, discontinuity condition, system boundary where power consumption of components are counted

Fig. 8 a 4 Gb/s eye-diagram.
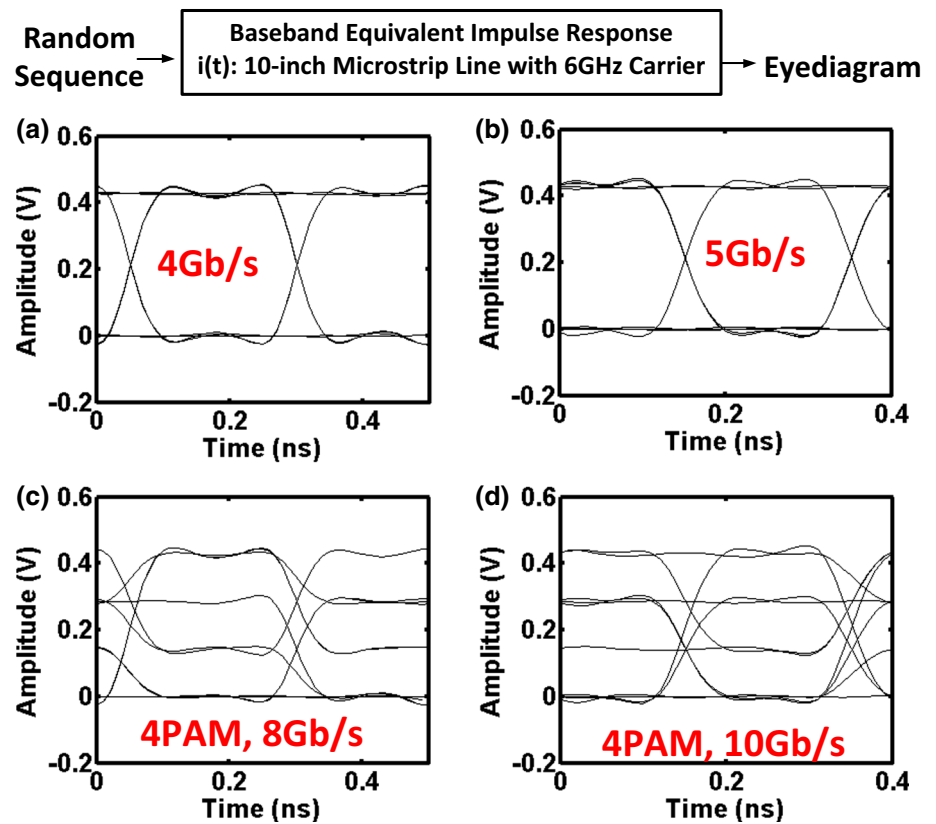b 5 Gb/s eye-diagram. c 4PAM,
8 Gb/s eye-diagram. d 4PAM,
10 Gb/s eye-diagram

Fig. 9 a Impulse response with
various carrier frequency.
b 9 Gb/s of eye-diagram when
carrier frequency is 10 GHz.
c 4PAM, 10 Gb/s eye-diagram
when carrier frequency is
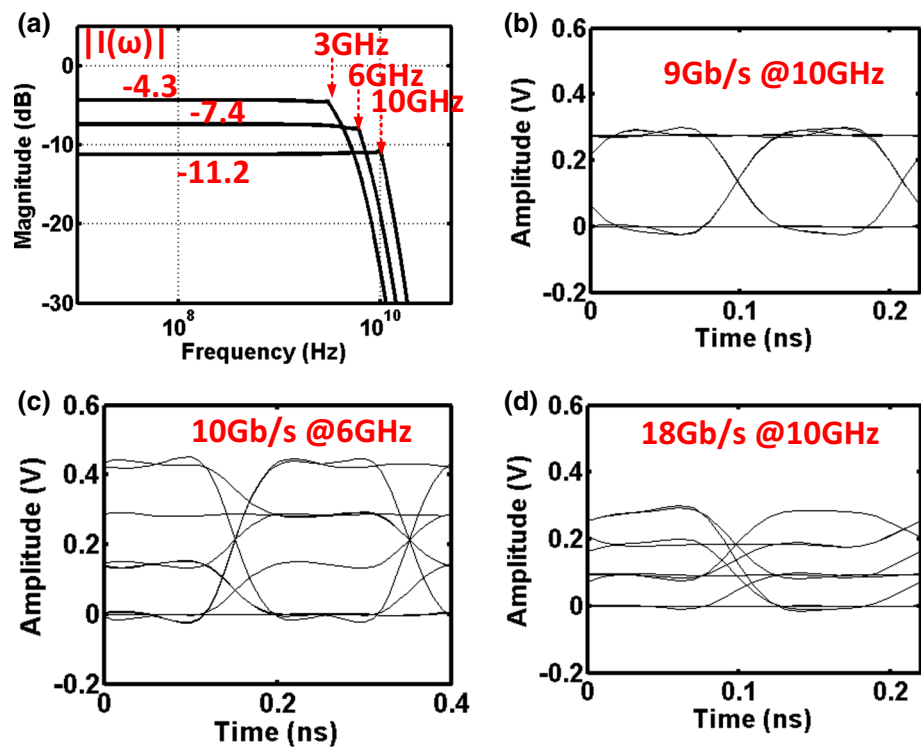6 GHz. d 4PAM, 18 Gb/s eye-
diagram when carrier frequency
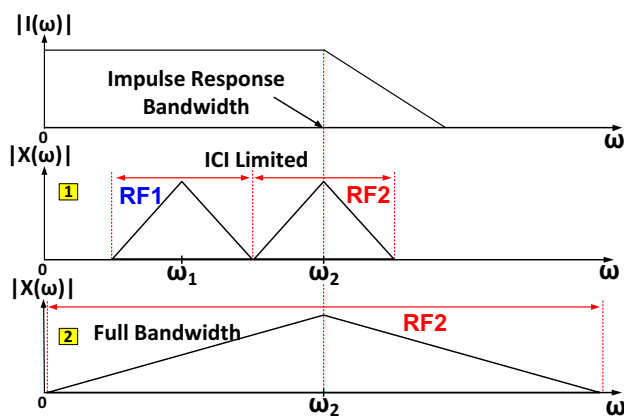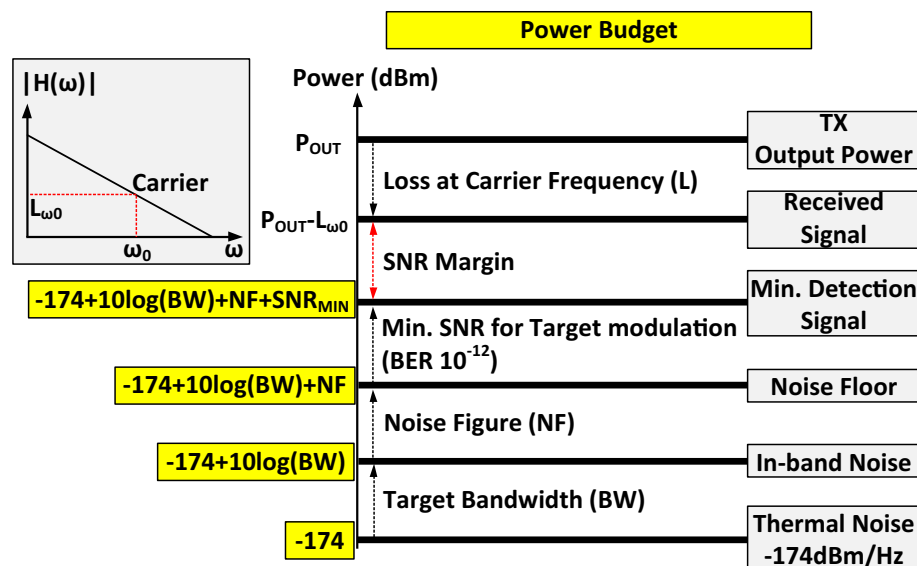is 10 GHz

Fig. 10 System power budget calculation

Fig. 11 Two RF channel versus one RF channel comparison when frequency response of transmission line has no discontinuity. The two RF channel case has bandwidth limitation based on ICI, but the one RF channel case can fully utilize the available bandwidth of baseband-equivalent impulse response

in energy calculation, and more. Rather, the above studies prove that 1.8 Gb/s of baseband signaling and possibly 16 Gb/s (because of ICI) of I and Q signaling at 10 GHz carrier frequency can be simultaneously transferred through a 10 in microstrip line without any aid of equalization scheme.

Based on this observation, two possible scenarios are drawn in Fig. 13 where MRFI can be deployed spectrally efficient. The first case is that, when the frequency response of channel rolls off, the data bandwidth of baseband signaling is limited at − 3 dB loss frequency, and on the top, an RF channel is inserted based on the power budget calculation. The second case assumes a channel exhibits much wider bandwidth than device technology can achieve (which would not occur very often). In other words, the bandwidth is limited by the bandwidth of device or

particular circuit topology (e.g. − 3 dB bandwidth of amplifier) itself. In this case, depending on the bandwidth of transmission line and bandwidth of RF channel, multiple RF carriers can be also deployed.

4 Frequency response with non-idealities

A baseband-equivalent impulse response of transmission line with non-idealities is studied in this section. As drawn with diagrams in Fig. 14(a) and measured frequency response of low-cost channel in Fig. 14(b), integrating transmission lines with circuit components requires connectors, vias, and wire-bonds that can create non-ideal effects such as destructive interference or impedance mismatch [30]. In typical situations, they limit the bandwidth of channel more definitively than conductive and dielectric loss. To study such effects, emulation and extraction of non-ideal characteristic is performed with the aid of HFSS (High-Frequency Structural Simulator) software.

4.1 Baseband-equivalent impulse response of frequency response with non-idealities

Although the proposed method is equally valid for measured frequency responses, simulation based calculations will be introduced because of flexibility in choosing parameters of transmission line. In order to emulate non-ideal channel conditions, particularly notches and ripples, a 10-in microstrip line [same parameters as Fig. 3(a)] is designed in HFSS with an intentional open-stub and intentional impedance mismatch at the input and output as shown in Fig. 14(c). Though not exactly same as the measured frequency response in Fig. 14(b), a similar

Fig. 12 a Loss versus distance at various frequency. b Frequency response of microstrip line with various length. The bandwidth of each length is estimated at − 3 dB loss frequency. c 14 Gb/s baseband-only signaling over 2 in microstrip line. d 3.7 Gb/s baseband-only signaling over 6 in microstrip line. e 1.8 Gb/s baseband-only signaling over 10 in microstrip line. f 18 Gb/s baseband-only signaling over 10 in microstrip line
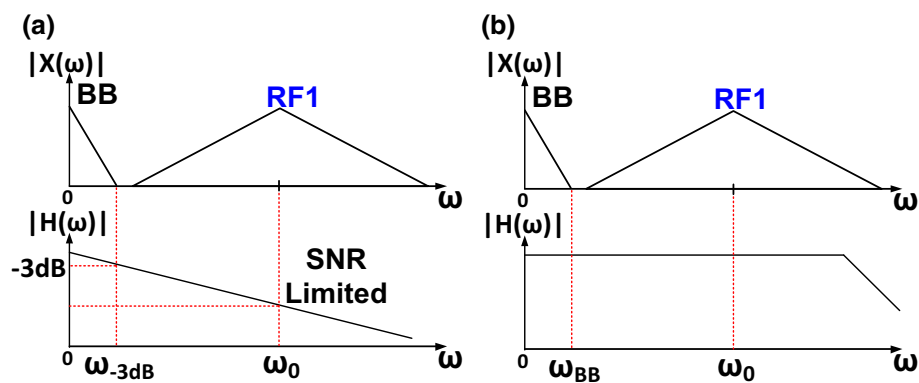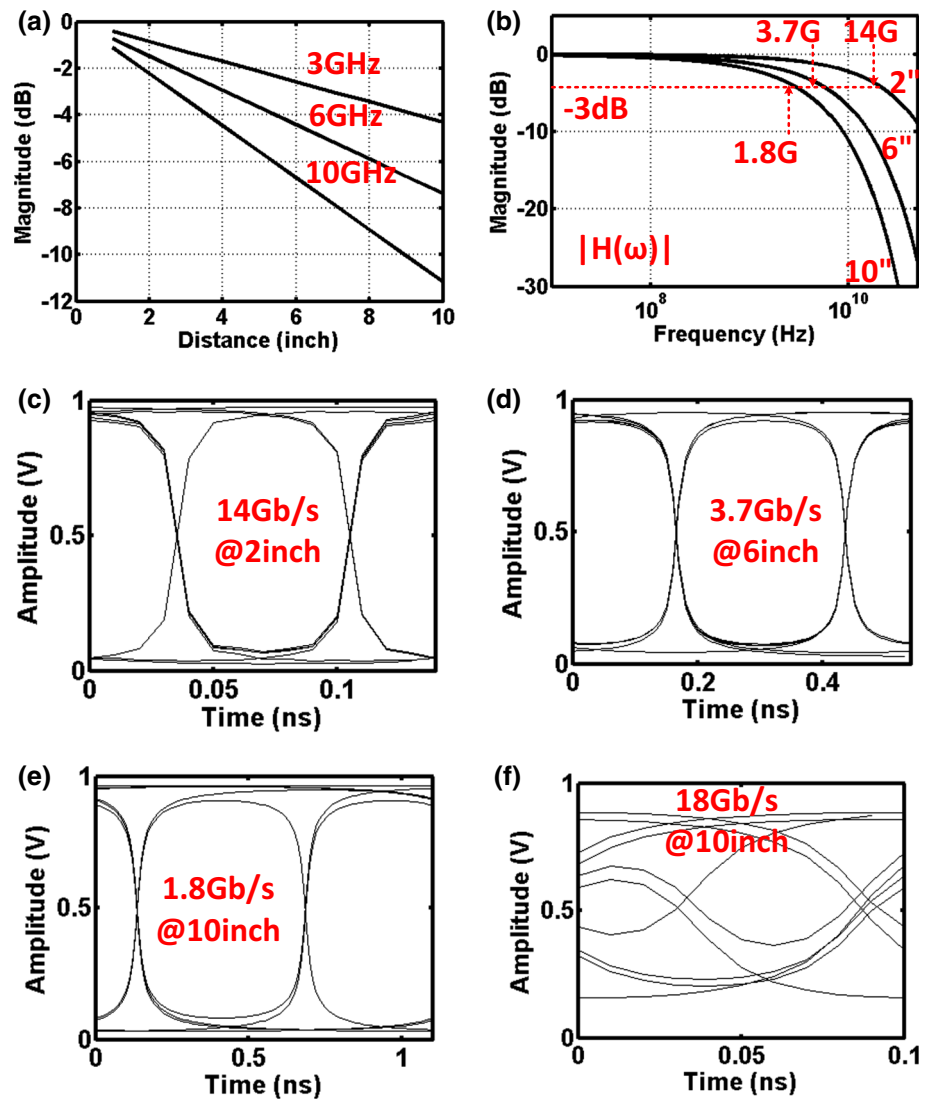
Fig. 13 Two possible cases of employing MRFI. a Bandwidth of baseband signaling is limited at 3 dB loss frequency, then carrier modulated RF channel is generated at the maximum possible frequency where SNR is limited. b If channel bandwidth is so wide, there is possible case when baseband electronics itself may cause bandwidth limitation depending on device technology. The baseband bandwidth is limited at this frequency and RF channel is employed additionally

Fig. 14 **a** Diagram of multi-drop bus, and low-cost channel configuration with chip integration. **b** Measured frequency response of low-cost channel. **c** HFSS model to emulate frequency notch. Impedance mismatch is added to have ripple effect in frequency response. **d** Magnitude response simulated from HFSS. **e** Calculated attenuation constant for 10-in distance. **f** Calculated propagation constant for 10-in distance
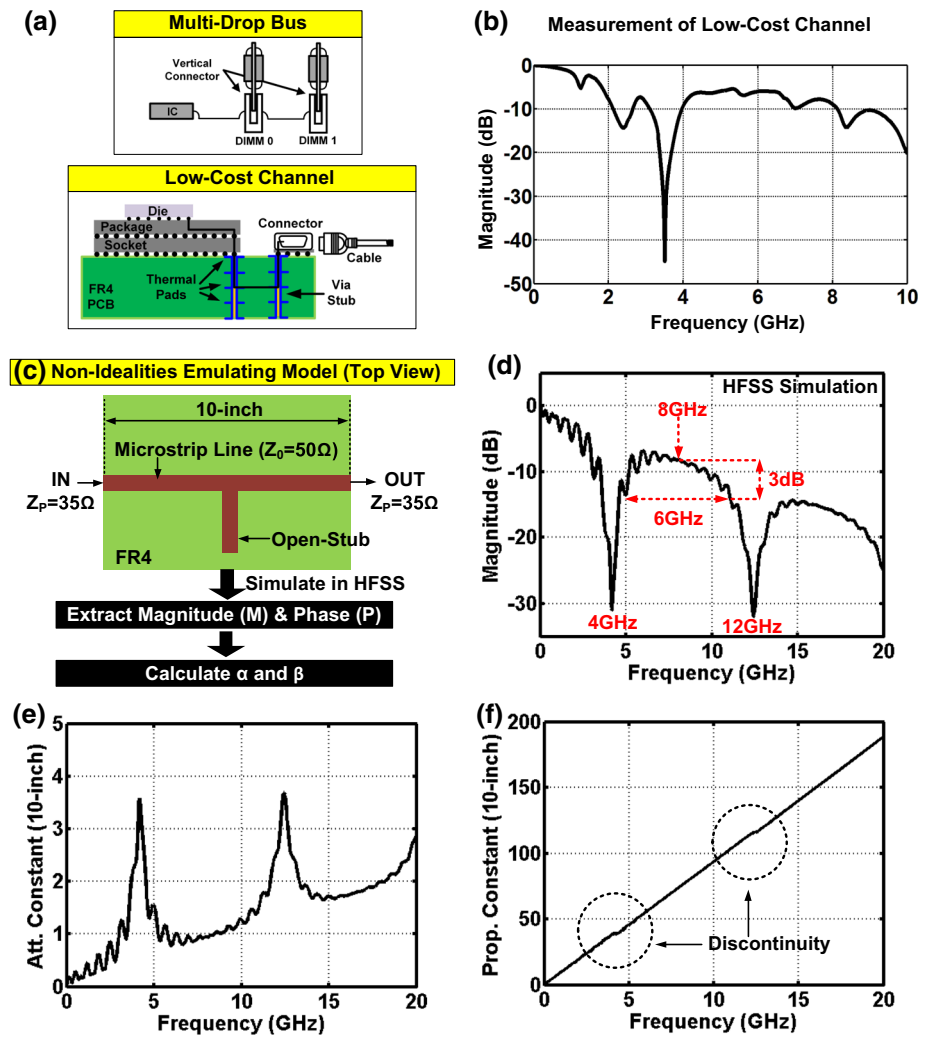
frequency response is created from HFSS simulation in Fig. 14(d). The location of notch frequency is adjusted by the length of open-stub, and the amount of ripple is controlled by the impedance mismatch between input/output port (Z_P) and characteristic impedance (Z_0). In this simulation, notches are created at 4 and 12 GHz, and consequently, 6 GHz of 3 dB bandwidth is observed centered around 8 GHz.

In order to come up with a baseband-equivalent impulse response of transmission line with non-idealities, attenuation constant and propagation constant are first calculated from the HFSS simulation by following method. From the definition of electromagnetic wave propagation in (3), each of magnitude and phase contribution can be written separately as,

$$e^{-\alpha(\omega)z1} = M \tag{24}$$

$$e^{-j\beta(\omega)z1} = P \tag{25}$$

$$\alpha(\omega)z_1 = -\frac{\log(M)}{\log(e)} \tag{26}$$

$$\beta(\omega)z_1 = -P \tag{27}$$

where M is the simulated magnitude in linear scale, and P is the simulated phase both extracted from HFSS. Then, using (26) and (27), the attenuation constant and propagation constant of 10-in microstrip line with non-idealities are plotted in Fig. 14(e, f). Notice that discontinuities can be found in the propagation constant around notch frequencies, which have profound effects after down-conversion for coherent systems (explained shortly).

Next, to utilize the maximum RF bandwidth for this non-ideal transmission line, a carrier frequency of 8 GHz is selected and its corresponding shifted frequency responses are plotted in Fig. 15(a). In this figure, the calculated attenuation and propagation constants in Fig. 14(e, f) are inserted into (19) and (20). Then using (22), a baseband-equivalent impulse response without the effect of LPF is plotted in Fig. 15(b). Also, the final baseband-equivalent

Fig. 15 a Frequency response shifted around carrier frequency 8 GHz. **b** Baseband-equivalent impulse response without LPF. **c** Baseband-equivalent impulse response with 4 GHz cutoff LPF. **d** Eye-diagram of 3 Gb/s. **e** Eye-diagram of 6 Gb/s with 4PAM. **f** Baseband-equivalent impulse response without LPF when only phase contribution is counted
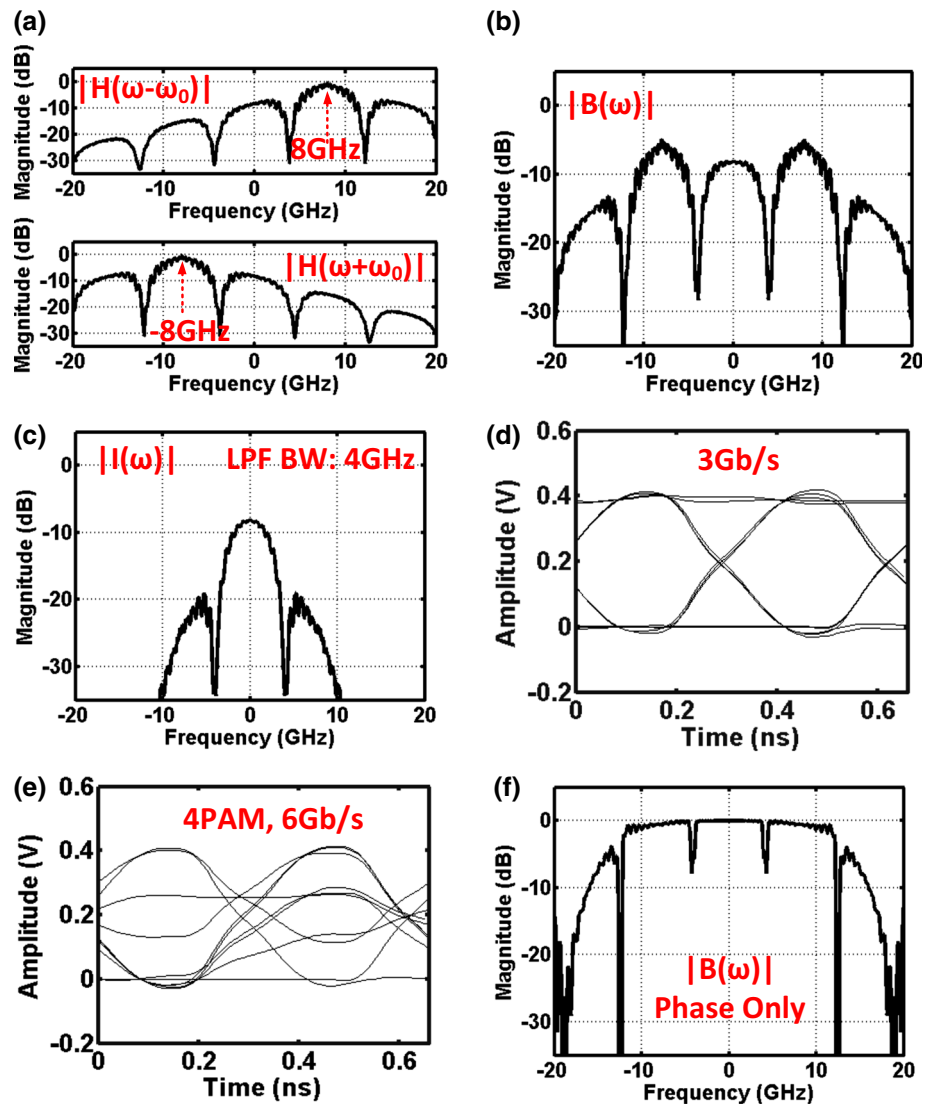
impulse response is shown in Fig. 15(c) after applying LPF with 4 GHz cutoff frequency. As indicated with 6 GHz of double-side bandwidth in Fig. 14(d), random sequences of 3 and 6 Gb/s with 4PAM signaling can be successfully transferred using 8 GHz carrier frequency in Fig. 15(d, e). In order to study the impact of phase discontinuity mentioned in Fig. 14(f), a new baseband-equivalent impulse response is written without the contribution of attenuation constant and LPF as if the transmission line is lossless.

$$B(\omega) = e^{-j\beta(\omega+\omega_0)}e^{+j\beta(-\omega_0)} + e^{+j\beta(\omega-\omega_0)}e^{-j\beta(\omega_0)} \qquad (28)$$

Interestingly in Fig. 15(f), the magnitude response of (28) also contains notches at 4 and 12 GHz. In the case of 4 GHz baseband-equivalent notch, 12 and 4 GHz signal components will land at 4 GHz and add themselves after down-conversion while carrier frequency is 8 GHz. In RF signal domain, because of the phase discontinuity in Fig. 14(f), the phase of combined 12 and 4 GHz signals

becomes close to 90° out of phase in relation to the phase of carrier frequency.

To study the effect of carrier frequency associated with notch frequencies, impulse responses without LPF for various carrier frequencies are plotted in Fig. 16. As expected, when carrier frequency is employed at the center of notch frequency, the baseband-equivalent impulse response would act as a high-pass filter as shown in Fig. 16(a). Impulse responses in Fig. 16(b–d) basically point out the importance of carrier frequency. Here, only (d) appears to be feasible for high-speed data transmission within available 3 dB bandwidth provided SNR is high enough.

Fig. 16 Various carrier frequency. **a** Impulse response without LPF at 4 GHz carrier. **b** Impulse response without LPF at 9 GHz carrier. **c** Impulse response without LPF at 13 GHz carrier. **d** Impulse response without LPF at 16 GHz carrier
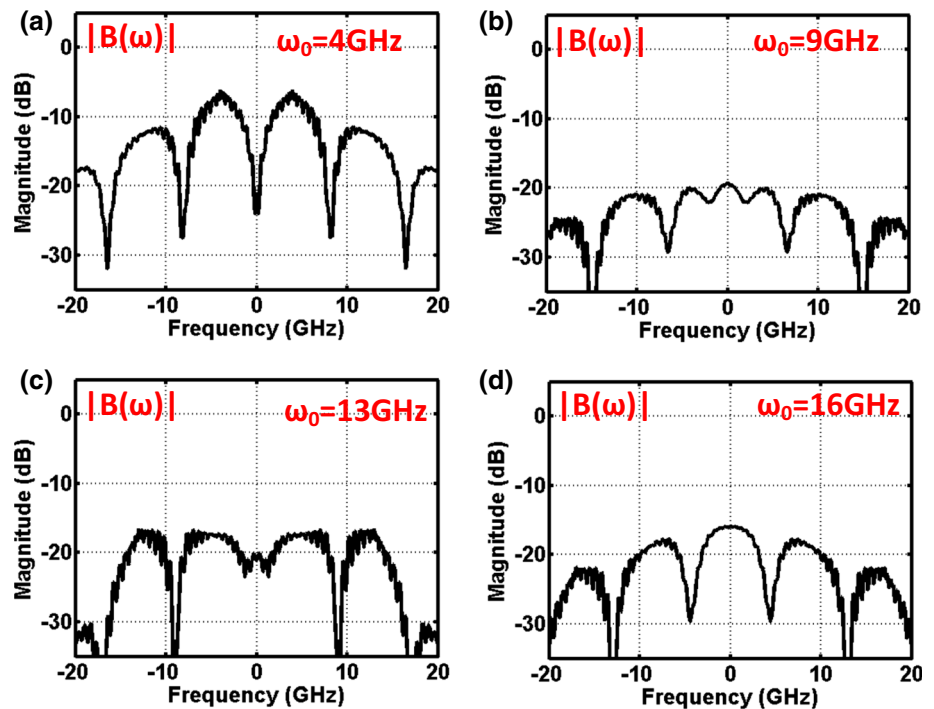
4.2 Tri-band RFI system implementation using 28 nm CMOS process for memory interface

A tri-band RFI system is implemented to enable 10 Gb/s data communication over 2-in microstrip line for memory interface, as shown in Fig. 17(a) [20]. In this design and experiment, notches are assumed to be generated at 1.5 and 4.5 GHz considering practical dimension ($\sim$ 1-in length) of multi-drop bus. Under this constraint, the baseband-signaling carries data strobe (DQS) and data mask (DM) signals by way of 4PAM modulation, and DQ1 through DQ8 are transmitted by 3 and 6 GHz carrier using 16QAM modulation with each DQ carrying 1.25 Gb/s of data bandwidth.

The target of the proposed system is to transfer 1-byte (8-bit) of high-speed data simultaneously over shared channel to reduce the number of pins while minimizing latency (maximum 1 DQS period) between transmitter and receiver for memory sub-systems [31]. Regardless of spectral efficiency, one could have chosen to serialize baseband data in baseband domain using serializer and de-serializer (SerDes) to transfer 1-byte of simultaneous data, but the latency penalty caused by clock and data recovery (CDR) becomes especially challenging as data rate increases. Instead, the proposed system serializes data strobe signal, data mask signal, and data all in frequency domain to remove the necessity of CDR such that the latency requirement is satisfied for memory sub-systems.

From a system hardware requirement point of view, even if the channel does not possess notches in frequency response, multiple RF channels may still be preferred over one RF channel in this 1-byte memory bus design. For instance, as opposed to the spectral efficiency argument of multi-band MRFI in Sect. 3.4, although one carrier is spectrally more efficient for transmission lines without non-idealities, the ultimate question becomes whether to design 64QAM with 1 carrier or 16QAM with 2 carriers for 1-byte transmission system. Arguably, the burden on circuit implementation for 64QAM is significant enough that one may prefer to implement a 2 carrier based RFI system.

Transistor-level simulation results (captured before ADC) show wide-open eye-diagrams of 4PAM signaling at each in-phase domain of 3 and 6 GHz carrier in Fig. 17(b). Impulse response based 4PAM simulations agree with the transistor level simulations except the fact that $2\omega_0$ component does not exist in the impulse response as shown in Fig. 17(c). The proposed architecture is fabricated in 28 nm CMOS process shown with a die-photo in Fig. 17(d). The measured spectrum of simultaneous tri-band transmission in Fig. 17(d), and eye-diagram and recovered DQS signal in Fig. 17(e) prove the concept and utility of the RFI system.
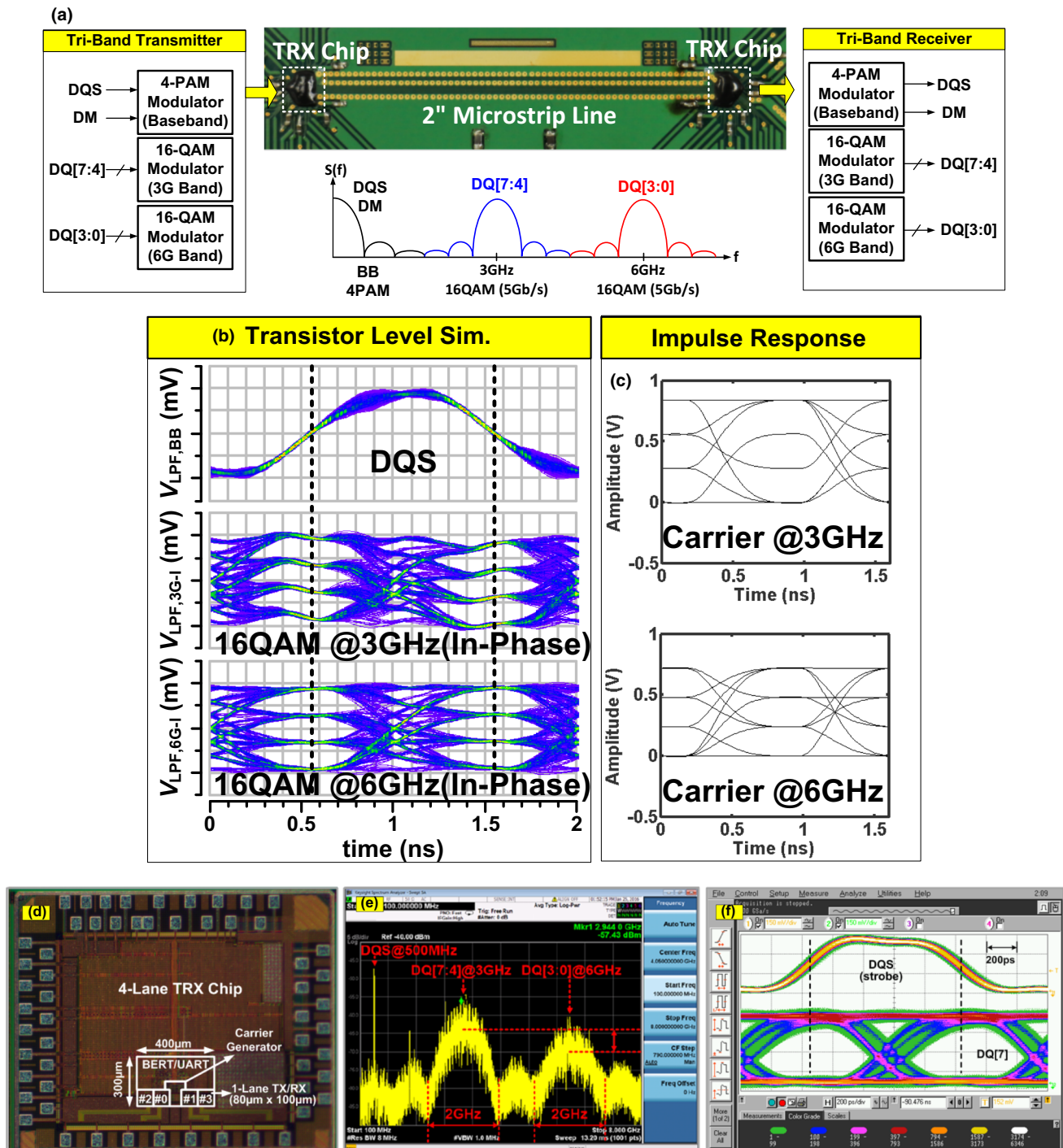
Fig. 17 a Tri-band (baseband, 3 GHz RF, 6 GHz RF) system implementation over 2-in PCB transmission line for memory interface application. Each 3 and 6 GHz carrier transfers 5 Gb/s data rate using 16QAM modulation. Data mask and data synchronization clock is transmitted using baseband signal with 4PAM modulation. **b** Transistor level 4PAM simulation for DQS, 3 GHz channel (in-phase), and 6 GHz channel (in-phase). **c** Impulse response based 4PAM simulation for 3 GHz channel and 6 GHz channel. **d** Implemented die-photo in 28 nm CMOS process. **e** Measured tri-band RFI spectrum. Data rate is 1G-baud, and the DQS clock speed is 500 MHz in this spectrum. **f** Measured eye-diagram after analog-to-digital converter

5 Conclusion

An explicit expression of baseband-equivalent impulse response in frequency domain for general transmission lines that support TEM mode of propagation is analytically derived. The frequency domain impulse response as a function of carrier frequency renders the estimation of equivalent bandwidth with indication of SNR trade-off. The impulse response reveals an equivalent pre-emphasis effect when the cut-off frequency of LPF after down-conversion is chosen properly.

Based on our explicit derivation in frequency domain, a time domain impulse response is established by taking an inverse Fourier transform. By way of time domain convolution, eye-diagrams are constructed with incoming random data sequences. In case of transmission lines without nonidealities, both frequency and time domain study suggests that only one carrier should be employed at the highest possible frequency within the SNR limit to achieve the most spectrally efficient MRFI architecture.

In order to study the baseband-equivalent impulse response of transmission lines with non-idealities, an emulation model is built in HFSS software by introducing intentional open-stub and impedance mismatch. The analysis guides how to compute attenuation and propagation constants with the help of HFSS simulations such that baseband-equivalent impulse response can be constructed by the same procedure developed in this paper. Impulse responses prove that the selection of carrier frequencies is crucial to achieve spectrally efficient multiband interconnect architecture.

References

1. Saltzberg, B. (1967). Performance of an efficient parallel data transmission system. *IEEE Transactions on Communications, 15*(6), 805–811.
2. Morgen, D. H. (1975). Expected crosstalk performance of analog multichannel subscriber carrier systems. *IEEE Transactions on Communications, 23*(2), 240–245.
3. Ahamed, S. V., Bohn, P. P., & Gottfried, N. L. (1981). A tutorial on two-wire digital transmission in the loop plant. *IEEE Transactions on Communications, 28*(11), 1554–1564.
4. Chow, P. S., Tu, J. C., & Cioffi, J. M. (1991). Performance evaluation of a multichannel transceiver system for ADSL and VHDSL services. *IEEE Journal on Selected Areas in Communications, 9*(6), 909–917.
5. Chow, P. S., Cioffi, J. M., & Bingham, J. A. C. (1995). A practical discrete multitone transceiver loading algorithm for data transmission over spectrally shaped channels. *IEEE Transactions on Communications, 43*(2), 773–775.
6. Barton, M., Chang, L., & Hsing, T. R. (1996). Performance study of high-speed asymmetric digital subscriber lines technology. *IEEE Transactions on Communications Conference, 44*(2), 156–157.
7. Amirkhany, A., Stojanovic, V., & Horowitz, M. A. (2004). Multitone signaling for high-speed backplane electrical links. In *IEEE Global Telecommunications Conference*, 2004.
8. Sartenaer, T., Vandendorpe, L., & Louveaux, J. (2005). Balanced capacity of wireline multiuser channels. *IEEE Transactions on Communications, 53*(12), 2029–2042.
9. Chang, M. C. F., Roychowdhury, V. P., Zhang, L., Shin, H., & Qian, Y. (2001). RF/wireless interconnect for inter- and intra-chip communications. *IEEE Proceedings, 89*(4), 456–466.
10. Gu, Q., Xu, Z., Kim, J., Ko, J., & Chang, M. C. F. (2004). Three-dimensional circuit integration based on self-synchronized Rf-interconnect using capacitive coupling. In *IEEE symposium on VLSI technology and circuits*, 2004.
11. Ko, J., Kim, J., Xu, Z., Gu, Q., Chien, C., & Chang, M. C. F. (2005). An RF/baseband FDMA-interconnect transceiver for reconfigurable multiple access chip-to-chip communication. In *IEEE solid-state circuits conference*, 2005.
12. Tam, S. W., Socher, E., Wong, A., & Chang, M. C. F. (2009). A simultaneous tri-band on-chip RF-interconnect for future network-on-chip. In *IEEE symposium on VLSI circuits*, 2009.
13. Byun, G., Kim, Y., Kim, J., Tam, S. W., Cong, J., Reinman, G., et al. (2011). An 8.4 Gb/s 2.5 pJ mobile memory I/O interface using bi-directional and simultaneous dual (Base + RF)-band signaling. In *IEEE Solid-State Circuits Conference*, 2011.
14. Kim, Y., Byun, G., Tang, A., Jou, C., Hsien, H., Reinman, G., et al. (2012). An 8 Gb/s/pin 4 pJ/b/pin single-T-line dual (Base + RF) band simultaneous bidirectional mobile memory I/O interface. In *IEEE international solid-state circuits conference*, 2012.
15. Jalalifar, M., & Byun, G. (2016). A 14.4 Gb/s/pin 230 fJ/b/pin/mm multi-level RF-interconnect for global network-on-chip communication. In *IEEE Asian solid-state circuits conference*, 2016.
16. Byun, G., Kim, Y., Kim, J., Tam, S. W., & Chang, M. C. F. (2012). An energy-efficient and high-speed mobile memory I/O interface using simultaneous bi-directional dual (Base + RF)-band signaling. *IEEE Journal of Solid-State Circuits, 47*(1), 117–130.
17. Kim, Y., Tam, S., Byun, G., Wu, H., Nan, L., Reinman, G., et al. (2012). Analysis of noncoherent ASK modulation-based RF-interconnect for memory interface. *IEEE Journal on Emerging and Selected Topics in Circuits and Systems, 2*(2), 200–209.
18. Ibrahim, S., & Razavi, B. (2009). Design requirements of 20-Gb/s serial links using multi-tone signaling. In *IEEE international symposium on circuits and systems*, 2009.
19. Cho, W., Li, Y., Kim, Y., Huang, P., Du, Y., Lee, S., et al. (2015). A 5.4 mW 4-Gb/s 5-band QPSK transceiver for frequency-division multiplexing memory interface. In *IEEE custom integrated circuits conference*, 2015.
20. Cho, W., Li, Y., Du, Y., Wong, C., Du, J., Huang, P., et al. (2016). A 38 mW 40 Gb/s 4-lane tri-band PAM-4/16-QAM transceiver in 28 nm CMOS for high-speed memory interface. In *IEEE solid-state circuits conference*, 2016.
21. Du, Y., Cho, W., Li, Y., Wong, C., Du, J., Huang, P., et al. (2016). A 16 Gb/s 14.7mW tri-band cognitive serial link transmitter with forwarded clock to enable PAM-16/256-QAM and channel response detection in 28 nm CMOS. In *IEEE symposium on VLSI circuits*, 2016.
22. Gharibdoust, K., Tajalli, A., & Leblebici, Y. (2015). Hybrid NRZ/multi-tone serial data transceiver for multi-drop memory interfaces. *IEEE Journal of Solid-State Circuits, 50*(12), 3133–3144.
23. Gharibdoust, K., Tajalli, A., & Leblebici, Y. (2016). A 4 × 9 Gb/s 1 pJ/b hybrid NRZ/multi-tone I/O with crosstalk and ISI reduction for dense interconnects. *IEEE Journal of Solid-State Circuit, 51*(4), 992–1002.
24. Pozar, D. M. (2005). *Microwave engineering* (Vol. 3). New York: Wiley.

25. Kim, Y., Nan, L., Cong, J., & Chang, M. C. F. (2013). High-speed mm-wave data-link based on hollow plastic cable and CMOS transceiver. *IEEE Microwave and Wireless Components Letter, 23*(12), 674–676.
26. Frans, Y., McLeod, S., Hedayati, H., Elzeftawi, M., Namkoong, J., Lin, W., et al. (2016). A 40-to-60 Gb/s NRZ transmitter with supply-regulated front-end in 16 nm FinFET. *IEEE Journal of Solid State Circuits, 51*(12), 3167–3177.
27. Bassi, M., Radice, F., Bruccoleri, M., Erba, S., & Mazzanti, A. (2016). A high-swing 45 Gb/s hybrid voltage and current-mode PAM-4 transmitter in 28 nm CMOS FDSOI. *IEEE Journal of Solid State Circuits, 51*(11), 2702–2715.
28. Han, J., Lu, Y., Sutardja, N., Jung, K., & Alon, E. (2016). Design techniques for a 60 Gb/s 173 mW wireline receiver frontend in 65 nm CMOS technology. *IEEE Journal of Solid State Circuits, 51*(4), 871–880.
29. Kocaman, N., Ali, T., Rao, L., Singh, U., Abdul-Latif, M., Liu, Y., et al. (2016). A 3.8 mW/Gbps quad-channel 8.5–13 Gbps serial link with a 5 tap DFE and a 4 tap transmit FFE in 28 nm CMOS. *IEEE Journal of Solid State Circuits, 41*(4), 881–892.
30. Du, Y., Cho, W., Huang, P., Li, Y., Wong, C., Du, J., et al. (2016). A 16-Gb/s 14-mW tri-band cognitive serial link transmitter with forwarded clock to enable PAM-16/256-QAM and channel response detection. *IEEE Journal of Solid State Circuits, 52*(4), 1111–1122.
31. Wang, D., Jacob, B., & Ng, S. (2008). *Memory systems: Cache, DRAM, disk*. San Francisco: Morgan Kaufmann.
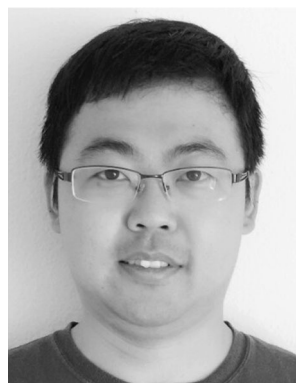
Yanghyo Kim completed his Ph.D. at University of California, Los Angeles in 2017. While he was working for Keyssa Inc. from 2010 to 2013, he commercialized the first 60 GHz CMOS contactless connector systems. He is now with the Jet Propulsion Laboratory as a postdoctoral fellow, developing CMOS system-on-chip (radar, radiometer, spectrometer) for space applications.

Wei-Han Cho received the B.S. and M.S. degrees (with Hons.) from National Tsing Hua University, Hsinchu, Taiwan, in 2008 and 2010, respectively. In 2016, he completed the Ph.D. degree at the Electrical Engineering Department, University of California, Los Angeles, CA, USA. His current research interests include energyefficient dense interconnect circuits. Dr. Cho was a recipient of the MOE Technologies Incubation Scholarship in 2013 and the UCLA EE Graduate Preliminary Exam Fellowship in 2014.

Yuan Du received the B.S. degree (with Hons.) in electrical engineering from Southeast University, Nanjing, China, in 2009, and the M.S. degree in electrical engineering from the University of California (UCLA), Los Angeles, CA, USA, in 2012. He completed the Ph.D. degree at UCLA, and now with Kneron Inc., San Diego, CA, USA, where he is involved in the hardware development. His current research interests include designs of domain-specific computing hardware accelerator, high-speed mixed-signal ICs, and CMOS RF ICs. Dr. Du was a recipient of the Microsoft Research Asia Young Fellowship in 2008, the Southeast University Chancellor's Award in 2009, and the Broadcom Fellowship in 2015.

Jason Cong received his B.S. degree in computer science from Peking University in 1985, his M.S. and Ph.D. degrees in computer science from the University of Illinois at Urbana-Champaign in 1987 and 1990, respectively. Currently, he is a Chancellor's Professor at the Computer Science Department, also with joint appointment from the Electrical Engineering Department, of University of California, Los Angeles, the director of Center for Domain-Specific Computing (CDSC), and the director of VLSI Architecture, Synthesis, and Technology (VAST) Laboratory. He served as the chair the UCLA Computer Science Department from 2005 to 2008, and is also a distinguished visiting professor at Peking University. Dr. Cong's research interests include synthesis of VLSI circuits and systems, programmable systems, novel computer architectures, nanosystems, and highly scalable algorithms. He has over 400 publications in these areas, including 10 best paper awards, two 10-Year Most Influential Paper Awards. He was elected to an IEEE Fellow in 2000 and ACM Fellow in 2008, and received two IEEE Technical Achievement Awards, one from the Circuits and System Society (2010) and the other from the Computer Society (2016).

Tatsuo Itoh received the Ph.D. degree in electrical engineering from the University of Illinois at Urbana–Champaign, Champaign, IL, USA, in 1969. He was with the University of Illinois at Urbana–Champaign, SRI, and the University of Kentucky, Lexington, KY, USA. In 1978, he joined The University of Texas at Austin, Austin, TX, USA, where he was a Professor of electrical engineering in 1981 and a Hayden Head Centennial Professor of Engineering in 1983. In 1991, he joined the University of California at Los Angeles, Los Angeles, CA, USA, as a Professor of electrical engineering and the TRW Endowed Chair of Microwave and

Millimeter Wave Electronics (currently the Northrop Grumman Endowed Chair). He has authored over 440 journal publications, 880 refereed conference presentations, and 48 books/book chapters in the area of microwaves, millimeter waves, antennas, and numerical electromagnetics. He has generated 80 Ph.D. students. Dr. Itoh is a member of the Institute of Electronics and Communication Engineers of Japan and the Commissions B and D of USNC/URSI. He was a recipient of the IEEE Third Millennium Medal in 2000, the IEEE MTT-S Distinguished Educator Award in 2000, the Outstanding Career Award from the European Microwave Association in 2009, the Microwave Career Award from the IEEE MTT-S in 2011, and the Alumni Award for Distinguished Service from the College of Engineering, University of Illinois at Urbana–Champaign in 2012. He was an elected member of the National Academy of Engineering in 2003. He served as the Editor of the IEEE TRANSACTIONS ON MICROWAVE THEORY AND TECHNIQUES from 1983 to 1985. He was the President of the IEEE MTT-S in 1990. He was the Editor-in-Chief of IEEE MICROWAVE AND GUIDED WAVE LETTERS from 1991 to 1994. He was elected as an Honorary Life Member of the MTT-S in 1994. He was the Chairman of Commission D of International URSI from 1993 to 1996. He served as a Distinguished Microwave Lecturer on Microwave Applications of Metamaterial Structures of the IEEE MTT-S from 2004 to 2006. He serves on the advisory boards and committees of a number of organizations.

Mau-Chung Frank Chang is currently the President of National Chiao Tung University, Hsinchu, Taiwan. He is also the Wintek Chair Professor of Electrical Engineering with the University of California, Los Angeles, CA, USA. His research interests include the development of high-speed semiconductor devices and high frequency integrated circuits for radio, radar, and imaging system-on-chip applications up to terahertz frequency regime. Dr. Chang is a member of the U.S. National Academy of Engineering, a fellow of the U.S. National Academy of Inventors, and an Academician of Academia Sinica of Taiwan. He was honored with the IEEE David Sarnoff Award in 2006 for developing and commercializing GaAs HBT and BiFET power amplifiers for modern high efficiency and high linearity smart-phones throughout the past 2.5 decades.